AIAA JOURNAL
Vol. 42, No. 4, April 2004

Reflection and Penetration of a Shock Wave Interacting with a Starting Vortex

Se-Myong Chang*
Kunsan National University, Chonbuk 573-701, Republic of Korea
Keun-Shik Chang†
Korea Advanced Institute of Science and Technology, Taejon 305-701, Republic of Korea
and
Soogab Lee‡
Seoul National University, Seoul 151-744, Republic of Korea

Experimental and numerical studies are conducted to investigate the interaction of a weak shock wave ($M_s = 1.22$) and a strong vortex ($M_{v,\max} > 1$). In terms of shock dynamics, two meaningful physics are observed from the experiment: reflected wave from the vortex edge and transmitted wave penetrating the vortex core. These weak waves are shown in the numerical interpretation to contribute to the emission of acoustic waves in shock–vortex interaction.

Nomenclature

A	=	accelerated wave
C	=	circumference centered on the vortex at the far field
C_+, C_-	=	characteristics
I	=	incident shock wave
K_+, K_-	=	invariant along characteristics
M	=	Mach stem in the shock reflection
M_s	=	moving shock Mach number
M_v	=	tangential Mach number around a vortex base on ambient speed of sound
$M_{v,\max}$	=	maximum rotational Mach number of the vortex, maximum M_v
U	=	faster or upper shock wave
$U_{\max}$	=	maximum tangential velocity in the shock–vortex interaction
p	=	pressure
R	=	reflected wave
r	=	radius distance from the vortex center
r_c	=	radius of the vortex core
S	=	slip line or slip layer
T	=	transmitted wave
V	=	main vortex
V_θ	=	tangential velocity
θ	=	azimuth angle or flow direction
ρ	=	density
Φ	=	angle of the incident shock wave

Subscripts

free	=	without disturbance
m	=	mean value along a circumference
s	=	ambient value behind the incident shock wave
u, l	=	upper (faster), lower (slower)
Δ	=	difference between two adjacent contours

Received 26 June 2001; revision received 2 January 2002; accepted for publication 9 July 2003.

*Assistant Professor, School of Mechanical Engineering. Member AIAA.
†Professor, Department of Aerospace Engineering. Member AIAA.
‡Associate Professor, School of Mechanical and Aerospace Engineering. Member AIAA.

Introduction

THE problem of shock–vortex interaction was first introduced in the 1950s by some researchers of fluid dynamics and acoustics.[1–4] Quadrupole noise has been known to be a key sound source of the screech tone in supersonic jets. The investigation of shock–vortex interaction also are a building block to understand more complex problems such as shock–boundary-layer interaction. In the 1960s, Dosanjh and Weeks approached this problem with a shock tube experiment and acoustic analogy.[5,6] Ribner's theoretical work[7] is also remarkable because it has succeeded to predict qualitatively the acoustic wave of the Dosanjh and Weeks[5] experiment, but his theory is only limited to the moderate range far from shock waves. More recently, many computational papers of the model study of shock–vortex interaction have been published thanks to the advances of numerical techniques.[8–10]

Ellzey et al.[9] pointed out that the shock–vortex interaction consists of two main categories: The shock wave is severely distorted by the surrounding flow, and the quadrupole sound is generated and propagated. The shock distortion effect is dominant at the earlier stage (or near field), whereas the sound is radiated at the later stage (or far field). This interpretation is supported and strengthened by other researchers in the series of papers.[11,12] The shock distortion and the quadrupole sound are the primary physics, but do not describe the interaction of a shock wave with a strong vortex entirely. Our question is what is the linkage between the two stages, and the objective of this study is to understand the mechanism how the shock wave produces acoustic waves. It is strange that no previous researchers took into account the strong vortex case where the maximum rotating vortex Mach number becomes supersonic ($M_{v,\max} > 1$): See the parameter domain in Fig. 1. That is, there may be some locally supersonic region in the strong vortex even though the ambient flow field is subsonic. In a recent paper,[13] some weak waves emitted in the interaction of a shock wave with a strong vortex are precisely traced without being neglected as noise. Reflection and penetration of the incident shock wave on a vortex was observed in both the experiment and computation. Our primary interest should be focused to the meaning of the weak waves.

In this study, the author proposes a simple experimental model of the interaction case of a weak shock wave ($M_s = 1.22$) and a strong vortex ($M_{v,\max} = 1.22$). The numerical solutions of Navier–Stokes equations are counterchecked with holographic interferograms and shadowgraphs. The emitted weak waves are precisely detected and traced to interpret the delicate flow physics.

Experimental Apparatus and Procedure

Figure 2 shows the experimental setup of the present problem. The author introduces an apparatus named shock splitter plate, transforming an incident shock ($M_s = 1.34$) into two planar shocks of different velocities: the faster one of $M_{su} = 1.41$ above the plate and the slower one of $M_{sl} = 1.22$ below the plate. The incident shock Mach number is measured by two pressure transducers mounted at the wall before the shock splitter.

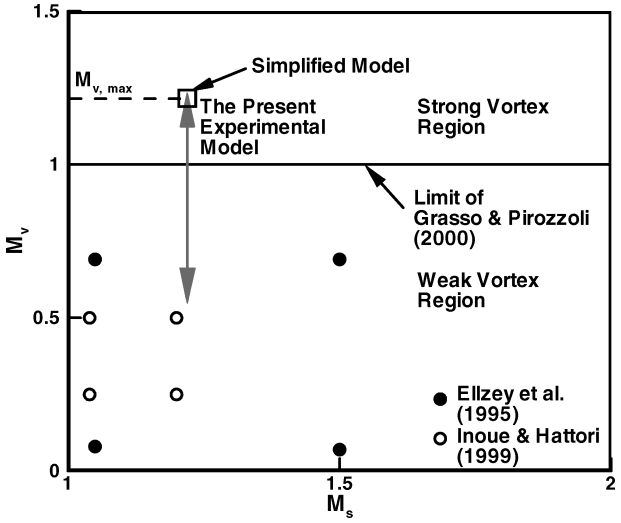

Fig. 1 Parameter plane of the present study and comparison with other research: strong vortex region extended to the supersonic range ($M_{v,\max} > 1$).

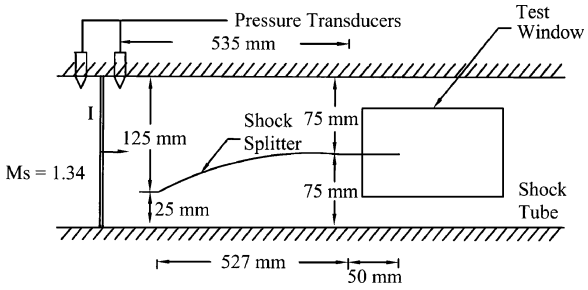

Fig. 2 Experimental setup of the present experimental model.

Design of the Shock Splitter

The contour of splitter plate is designed for the purpose of splitting the incident shock into two plane shock waves with minimum disturbance by the method of characteristics based on Witham's ray shock thory.[14] The procedure of drawing the lower part is similar to the rocket nozzle design in supersonic flow.

When the incident shock enters the inlet of the lower part in Fig. 3a, the incident flow induced by the moving shock undergoes a sudden expansion at point O. K_+ is constant along the C_+ characteristics OA,

$$K_{+OA} = \theta_O + \omega_O = \theta_A + \omega_A \tag{1}$$

Similarly, along the C_- characteristics AB,

$$K_{-AB} = \theta_A - \omega_A = \theta_B - \omega_B \tag{2}$$

The flow is tangential near the wall without considering viscosity, $\theta_A = 0$. Our objective is to achieve a parallel flow at point B, $\theta_B = 0$. Then, simplifying Eq. (1) and (2), we get the following relation:

$$\theta_O = \omega_B - \omega_O = \int_{M_{sO}}^{M_{sB}} \left[\frac{\lambda(M)}{M^2 - 1}\right]^{\frac{1}{2}} \mathrm{d}M \tag{3}$$

where

$$\lambda(M) = \left(1 + \frac{2}{\gamma + 1}\frac{1 - \mu^2}{\mu}\right)\left(1 + 2\mu + \frac{1}{M^2}\right)$$

$$\mu^2 = \frac{(\gamma - 1)M^2 + 2}{2\gamma M^2 - (\gamma - 1)}$$

The design values are $M_{sO} = M_s = 1.34$ (inlet) and $M_{sB} = M_{sl} = 1.2$ (outlet). When they are substituted in Eq. (3), $\theta_O = -21$ deg is obtained. The negative sign indicates that the deflection angle should be expansive.

At all of the node points, we set a system of simultaneous equations such as Eq. (1) and (2) and solve them from the known points in Fig. 3a. We may solve the unknown point D from the known O and E, for example. The slopes of characteristics are

$$\mathrm{OE}(C_+): \left(\frac{\mathrm{d}y}{\mathrm{d}x}\right)_{OE} = -\frac{1}{2}[\tan(\theta_O + m_O) + \tan(\theta_E + m_E)] \tag{4}$$

$$\mathrm{ED}(C_-): \left(\frac{\mathrm{d}y}{\mathrm{d}x}\right)_{ED} = -\frac{1}{2}[\tan(\theta_E - m_E) + \tan(\theta_D - m_D)] \tag{5}$$

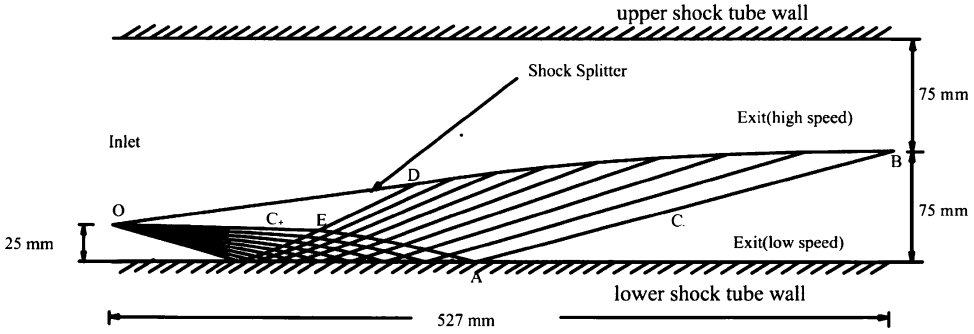

a) Method of characteristics

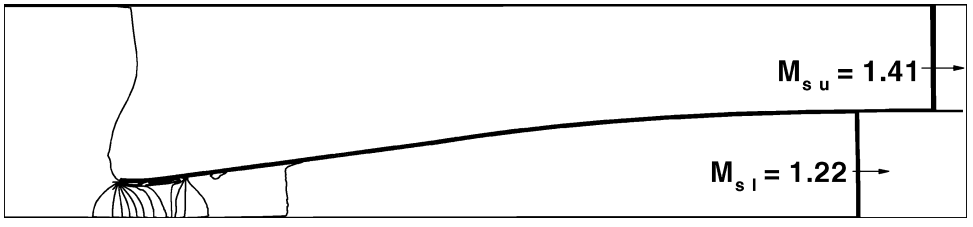

b) Density contours obtained from the Navier–Stokes simulation

Fig. 3 Design of a shock splitter.

where

$$m = \tan^{-1}\left[\frac{M^2 - 1}{M^2\lambda(M)}\right]^{\frac{1}{2}}$$

The contour ODB drawn from the characteristics curves is composed of C_+ and C_-: (Fig. 3a). The splitter plate has a uniform thickness of 1 mm. Figure 3b is the Navier–Stokes simulation of the designed splitter: The resultant shock strengths are $M_{su} = 1.41$ and $M_{sl} = 1.22$. The difference from the design value ($M_{sl} = 1.2$, 1.6% error) may be regarded as the viscosity effect. The author used Fig. 3b data as the initial condition of the numerical simulations.

Procedure of the Experiment

The upper shock in Fig. 3b is diffracted at the trailing edge of splitter plate, generating a strong starting vortex. The lower shock arrives later to strike the vortex at 137 μs after the upper shock diffraction. A shock tube of 60×150 mm cross section is used in the experiement.[13] The driver and driven gases are all dry air under standard atmospheric conditions.

To visualize the instantaneous density field of the compressible flow, double-exposure holographic interferometry is used in addition to shadowgraphy.[13,15] The fringes are made by interference of the two duplicated pulse laser beams: One records the image of undisturbed test section, and the other seizes on the disturbed flow in some hundreds of microseconds. When the holography film is projected with a reference He–Ne laser, the interferogram in black and white fringes is finally reconstructed.

Numerical Simulations

The visualized results are crosschecked with the numerical solution of the Navier–Stokes equations of conservative integral forms (see Ref. 16). The boundary conditions in a standard form are adopted: no-slip condition at walls and characteristic boundary condition to preserve the Riemann invariant at inlet and outlet. The initial condition is obtained from the full simulation including the shock splitter plate (Fig. 3b). The simulation is performed with a total variation diminishing method based on Roe flux difference scheme with MUSCL expansion, and the accuracy is second order in time and third order in space. The viscous flux is added with simple central differences of conservative variables, and the wall temperature is fixed as a boundary condition.

Such second or third orders of accuracy can be sometimes insufficient in the delicate computation like acoustic wave problems, but a locally finer grid will compensate for this drawback using the quadrilateral unstructured adaptive grid system (QUAG).[17,18] The adaptive method uses a refinement and unrefinement algorithm in accordance with error levels. The error indicator is the gross velocity difference of a cell with its adjacent cells. A cell is refined when the error exceeds the error level, and vice versa. The unstructured data structures of quadtree and linked list are used in the storage of complicated cell connectivity. In the present problem, four to six error levels were used to catch the shock waves and the weak waves. Figure 4a is a typical example of the adaptive grid system of four levels. At a glance, the wave and vortex structure can be discerned from the finer grid region in Fig. 4a.

Computational Validation

To validate our computational code, a classical problem is solved in Figs. 4a–4d. This is the interaction problem of a shock and a weak vortex.[5–7,9] The initial data are $M_s = 1.29$, $U_{\max} = 177$ m/s ($M_v = 0.52$), and $r_c = 2.77$ mm. The computational domain is a 75×75 mm rectangle, and the primitive Rankin vortex model is

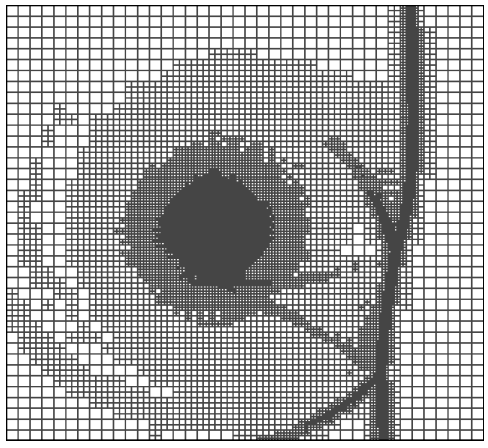

a)

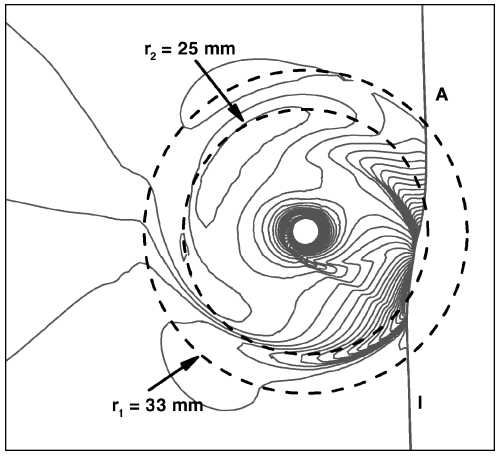

b)

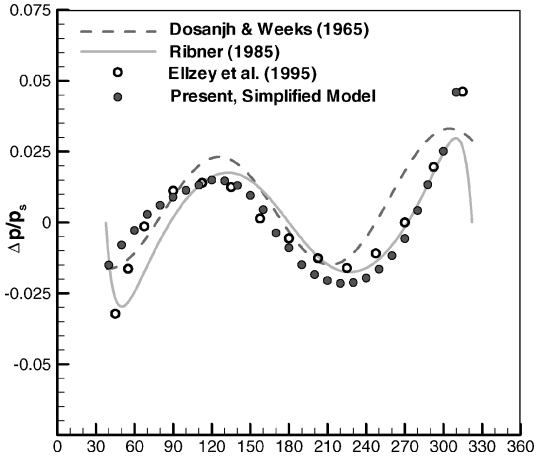

c)

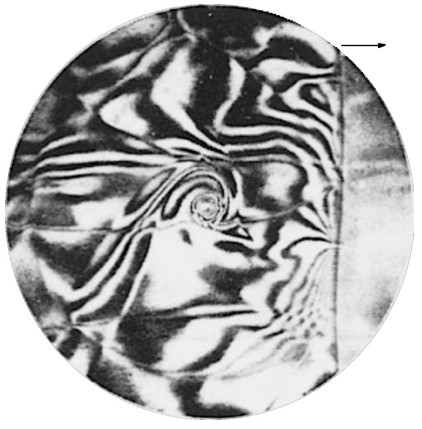

d)

Fig. 4 Dosanjh and Weeks[5] problem: a) quadrilateral unstructured adaptive grids (four levels, partial view), b) density contours around the vortex 78 μs after the shock passes through the vortex center, c) acoustic pulse pressure distribution along the circumferences in shown in b), and d) Mach–Zehnder interferogram.

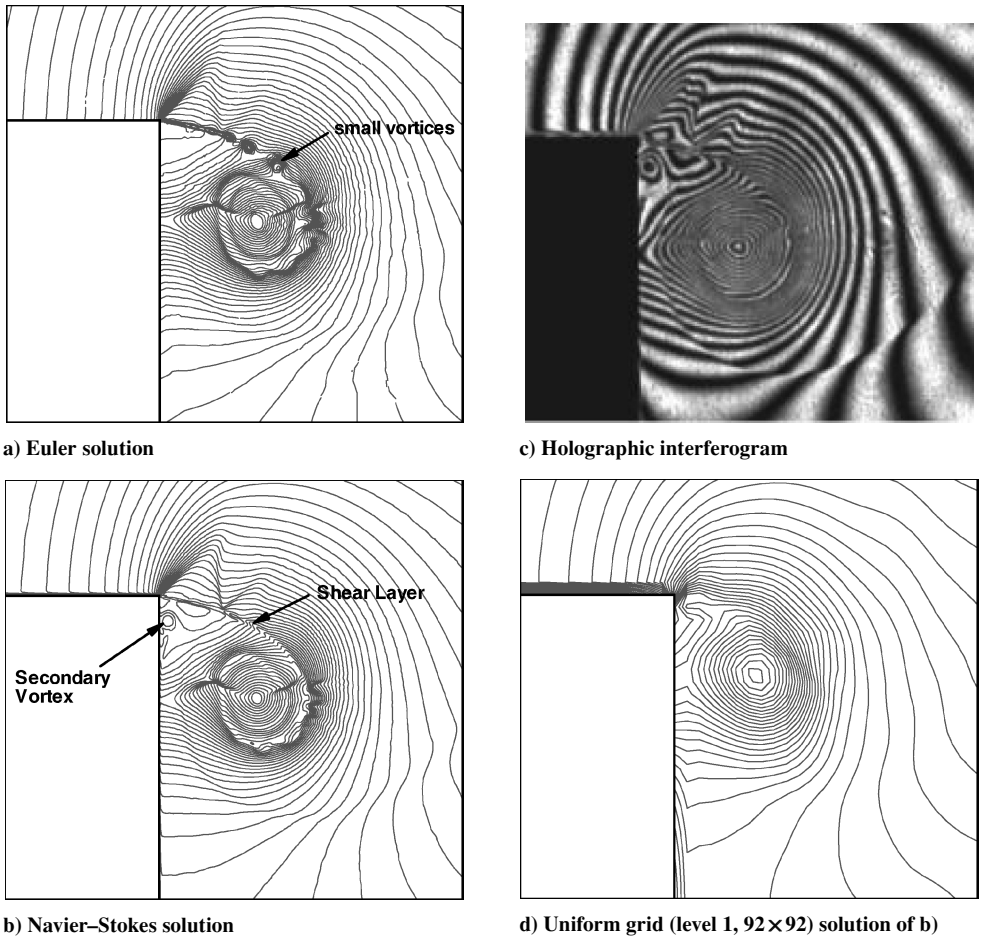

a) Euler solution

c) Holographic interferogram

b) Navier–Stokes solution

d) Uniform grid (level 1, 92×92) solution of b)

Fig. 5 Shock diffraction in the 90-deg corner.

used for the description of initial condition inside a vortex:

$$V_{\vartheta,\text{free}}(r) = \begin{cases} U_{\max}(r/r_c), & r \le r_c \\ U_{\max}(r_c/r), & r \ge r_c \end{cases} \tag{6}$$

Because there is no artificial coefficient to isolate the vortex at the outer region ($r \ge r_c$) in Eq. (6), the planar incident shock wave should be initially placed at least as far as $x = -20r_c$ to avoid parasitic numerical waves. Figure 4b shows the density plot at 78 μs after the incident shock passes through the initial position of vortex center. Along the two circumstance r_1 (precursor) and r_2 (acoustic), the pressure distribution vs θ is sampled, and the difference of two pressures is plotted in Fig. 4c, where various results of other researchers are also provided. The present simulation shows good agreement with experiment,[5] theory,[7] and other computation.[9] An experimental photograph[5] in Fig. 4d also gives a qualitative validation of this computational method: Compare it with Fig. 4b.

Effect of Viscosity and Convergence

The Navier–Stokes equations are solved in this study, and therefore, the viscosity effect is considered here. Inviscid computation or Euler equations also give us the information of the wave physics, but for the problems including shear layer, the viscosity cannot be neglected.

Figures 5a–5d show an example of the shock diffraction over a 90-deg sharp corner. The incident Mach number is $M_s = 1.5$ and Reynolds number, $Re = 1 \times 10^6$ based on the shock-induced flow speed and the entrance width. In the Euler solution, Fig. 5a, small vortices due to the Kelvin–Helmholtz instability are formed on the slip layer. However, in Fig. 5b, the Navier–Stokes solution with constant wall temperature shows no small vortex on the slip layer because they are diffused by the viscosity effect. The secondary vortex generated by the boundary layer separation at the vertical wall can be observed only in the viscous solution. The experimental result in Fig. 5c apparently reveals that the Navier–Stokes result is very similar to the real physics.

Another question about code performance is the convergence problem. In Figs. 5a and 5b, the adaptation level of grids is five to catch the delicate fluid elements. Figure 5d is the level one (or uniform) grids Navier–Stokes result, and we can see that coarse or fine grids just have influence on the resolution without violation of convergence, when compared with Fig. 5b.

Results and Discussion

Six representative frames (shadowgraphs) of the experiment are displayed in sequence in Figs. 6a–6f. The time given in the Fig. 6 caption is counted from the estimated instant of the first diffraction of upper shock U. In Fig. 6a, U is already diffracted at the aft tip of the plate, and a strong starting vortex V is generated. The lower incident shock I is shown just before striking the vortex V in Fig. 6b. The slower shock I seems to be thicker than the faster shock, U in the shadowgraphs due to the aeroelastic vibration effect of the flat plate. In the earlier stage of shock–vortex interaction, the upper part of I is severely distorted by the clockwise rotation of V, as shown in Fig. 6c. In Fig. 6d, part of I (between the plate and V) is accelerated to split to a kidney bean shape while one end of the rest of part I is seized by the vortex. The accelerated wave A is propagated to the radial direction, and the decelerated part of I is rotated in the counterclockwise direction (Figs. 6e–6f).

In the later photographs of Figs. 6d–6f, there are a few waves we cannot yet clearly understand. Among them, two meaningful weak waves are extracted: they are the reflected wave R and the transmitted wave T. In Figs. 6d and 6e, it is observed that R is merged to a part of A. The shock I penetrates the vortex core, showing a faint vestige of T connected with a spiral tail in Fig. 6e, but it disappears in Fig. 6f.

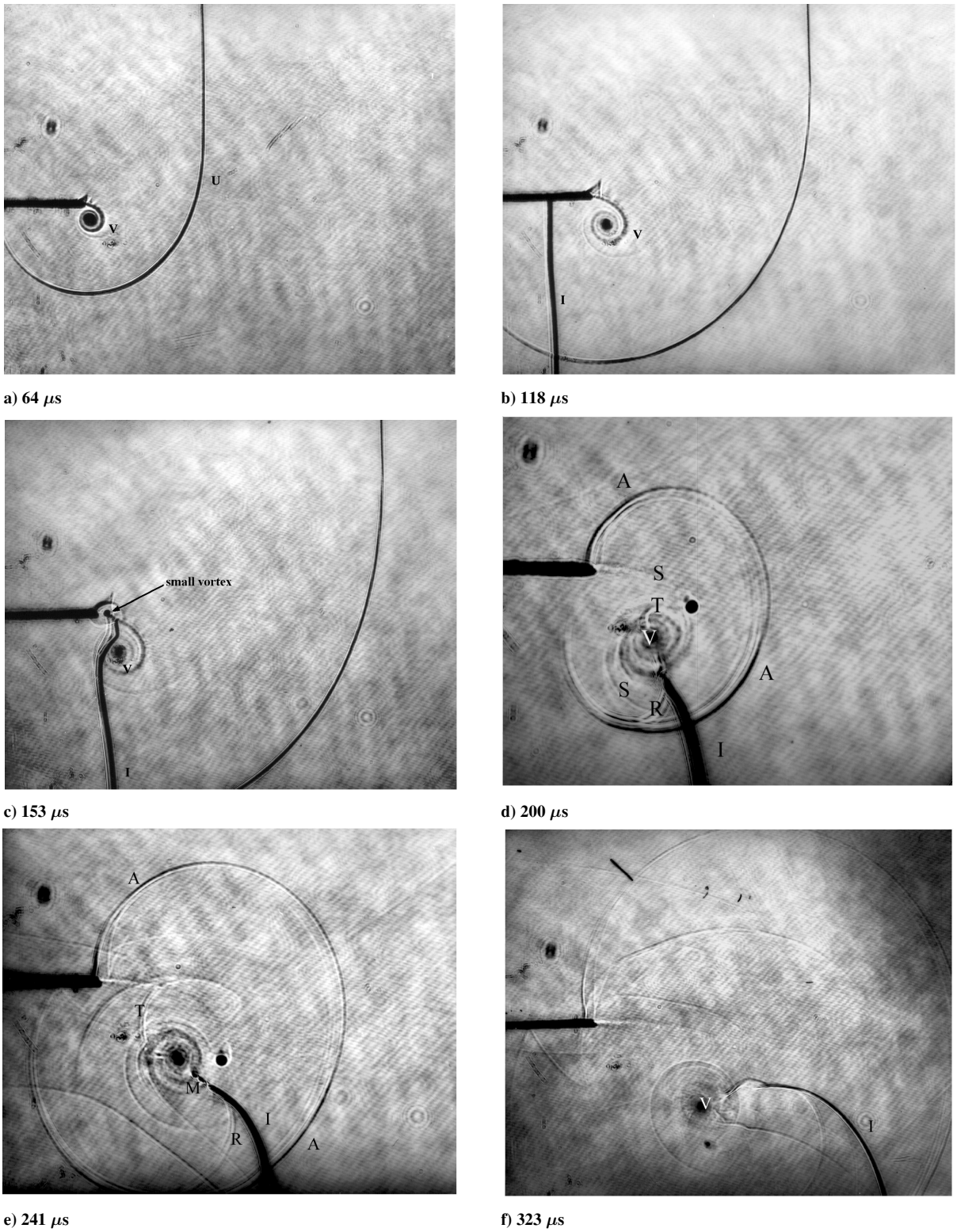

Fig. 6 Experimental shadowgraphs of weak shock and strong vortex interaction.

The complement computations for the scene between Figs. 6b and 6d are arranged in Figs. 7a–7f. The computational domain is 250×150 mm, where the tip of plate is placed at 100 mm from the left inflow boundary (Fig. 2), and the initial conditions are induced from Fig. 3b. The refinement level of the adaptive grids is six.

The incident shock is diffracted at the aft tip of plate in Fig. 7a, where the main vortex V is connected with spiral slip lines S. Figure 7b shows the genesis of the small vortex produced by the same principle as the generation of the main vortex in Fig. 6a. However, the rotational direction of this small vortex is opposite to that of V. In Fig. 7c, the diffracted shock A_1 is propagated to the radial direction from the source (the center of small vortex) while the upper part of I, A_2, penetrates the vortex core. The two waves, A_1 and A_2, will be merged to the accelerated wave A in Figs. 7d and 7e, where the shock I is severely distorted to make a reflection at the slip layer of the vortex edge. In Fig. 7e, the reflected wave R is formed more clearly, and the upper tip of I, M, is deflected by the clockwise rotation of vortex. The strong wave M penetrates the vortex core again, T, but the strength of this secondary wave seems very weak. The accelerated wave A consists of two parts, A_1 and A_2 in Fig. 7e,

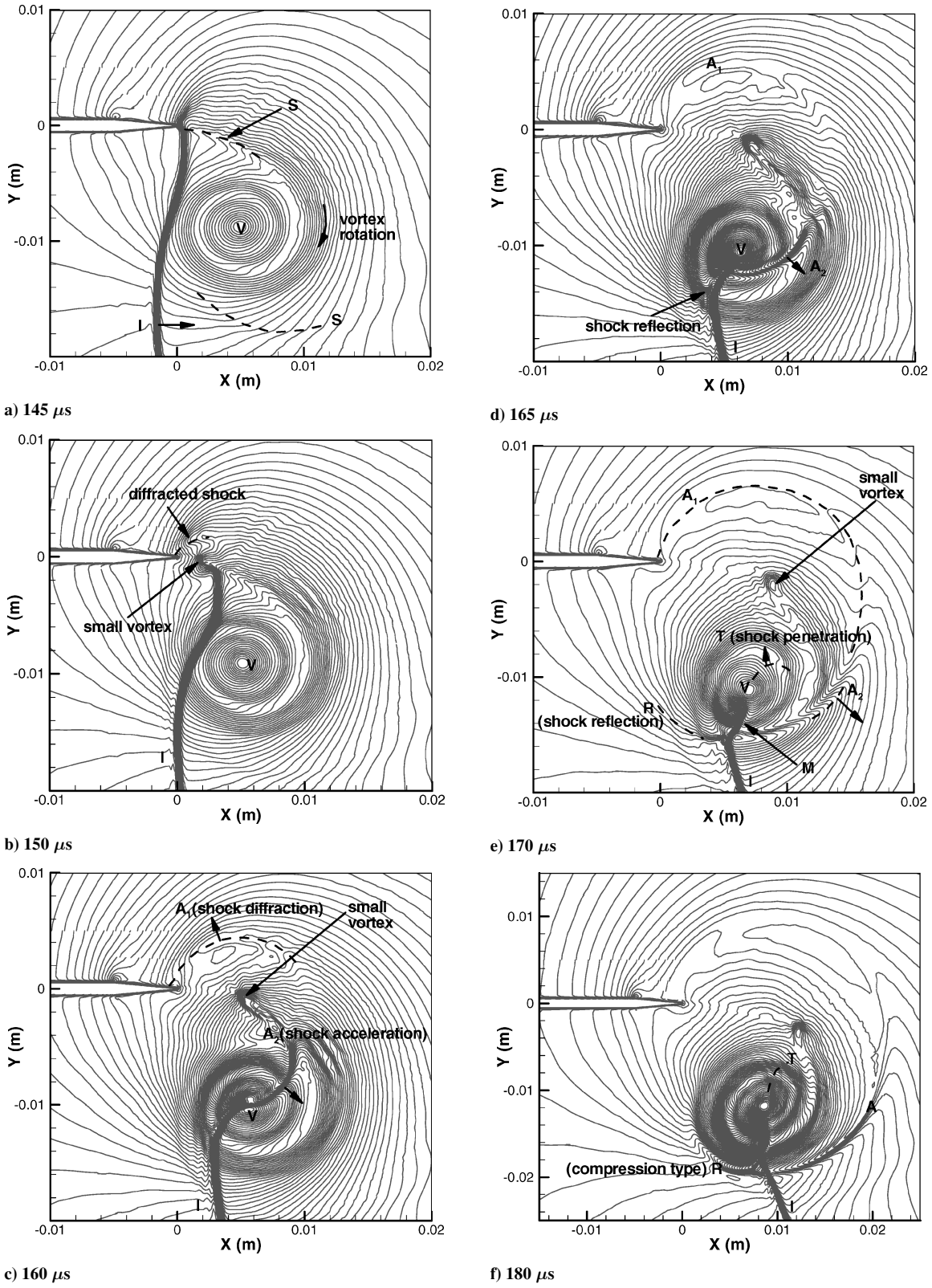

Fig. 7 Navier–Stokes simulation for this experimental model.

and the reflection R is soon merged to A (Fig. 7f). The transmitted wave T is still weak but beginning to slightly deform the density contours inside the vortex.

Shock Reflection and Shock Penetration

The experiment and numerical simulation are compared in Figs. 8a–8d. In the holographic interferogram and the numerical density plot, Figs. 8a and 8b show the earlier stage, whereas Figs. 8c and 8d show the later stage. The density scale is $\Delta\rho = 0.025$ kg/m^3.

The reflected wave R pattern in Fig. 8 is shown schematically in Fig. 9. R can be interpreted as the reflection of I at the slip layer of vortex edge. As shown in Figs. 9a–9c, there are two possible patterns of shock reflections from the slip layer: the compression type (earlier stage; Figs. 8a and 8b and Fig. 9b) and the expansion type (later stage; Figs. 8c and 8d and Fig. 9c). The difference of the two types depends on the incident angle Φ of I on the slip layer S. Because the vortex core rotates like a solid body, the transformed shock morphology in the left of Figs. 9b and 9c shows that R is compression

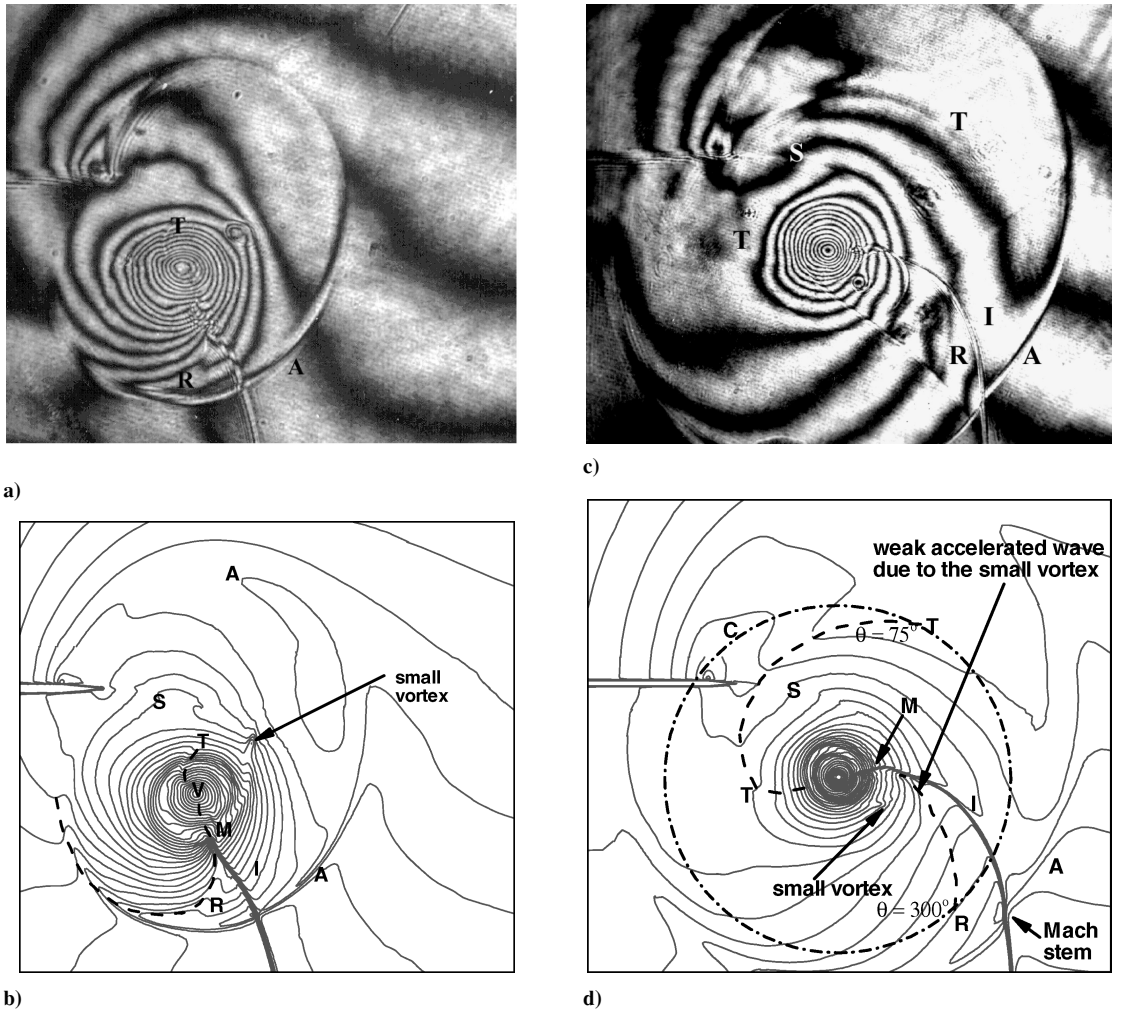

Fig. 8 Comparison of a) holographic interferogram, 200 μs; b) Navier–Stokes simulation, 200 μs; c) holographic interferogram, 268 μs; and d) Navier–Stokes simulation, 268 μs.

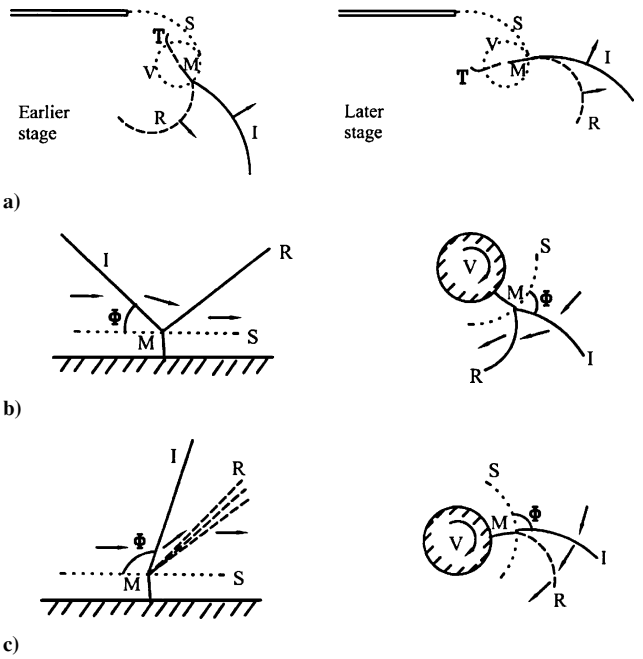

Fig. 9 Schematic diagram of reflected wave: a) two stages of experimental model, b) earlier stage or compression-type reflection ($\Phi < 90$ deg), and c) later stage or expansion type reflection ($\Phi > 90$ deg).

if $\Phi < 90$ deg and expansion if $\Phi > 90$ deg. The compression type is very similar to a single Mach reflection except that the Mach stem M is immerged under the slip line S. However, S is very diffused by flow viscosity to a thick layer in the real physics.

The reflection is generally transitional from compression to expansion as shown in Fig. 9a. If a fluid particle passes through a wave, and the pressure is increased/decreased, then the wave is compressive/expansive. This fact has been checked in the numerical data of Fig. 8b and 8d.

Returning to Fig. 8, we see the transmitted wave T induced by M penetrating the vortex core. T is very weak and blurred to compression wave at the later stage, and with wave R, it constructs the spiral structure such as in Fig. 10. R and T are attached to the vortex core because the vortex is strong enough to catch the weak waves. As the incident shock I goes counterclockwise, the spiral tails of weak waves also rotate in the similar manner. The R part (dashed line in Fig. 10) is merged with the accelerated wave A, forming the kidney bean shape. Wave A is composed of at least three wave components: the diffracted shock A_1, the accelerated shock A_2, and the reflected wave R (Fig. 7f).

Experimental Model Discussion

In this paper, a new experimental model to generate a shock–vortex interaction has been introduced. This model differs from the shock interaction with an isolated vortex in previous studies.[5–9] The starting vortex is connected with the trailing edge of plate by a slip layer (Fig. 7a). Its shape is far from the tangential uniformity or axisymmetry often assumed in the simplified model study. Figure 11

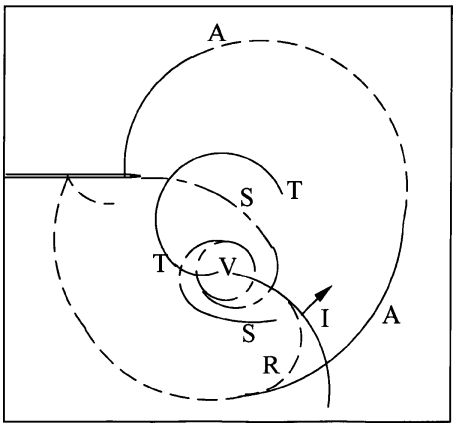

Fig. 10 Schematic of experimental model: weak waves *R* and *T* propagate counterclockwise with the spiral wavefronts (also see Fig. 6e): ——, compression wave; – – –, expansion wave; and – · –, slip layer.

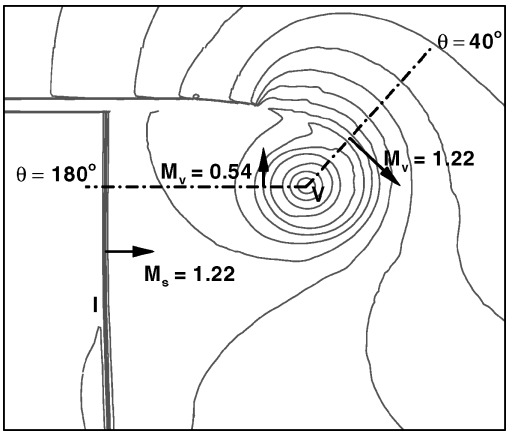

Fig. 11 Structure of free vortex in experimental model: equivalent to about Fig. 6b.

shows that definition of r_c and $U_{\max}$ (or M_v) is not easy for the real vortex. Along the $\theta = 40$ deg line, the maximum M_v is 1.22 (supersonic), but along the $\theta = 180$ deg line, it is 0.54 (subsonic). Therefore, M_v cannot be fixed in this experimental model, as marked in the arrow-lined range in Fig. 1.

The vortex in this study is a strong one, which means that there is a supersonic region ($M_{v,\max} > 1$) inside the flowfield. As shown in Fig. 1, these kinds of flow regimes have not been seriously investigated so far. The existence of a supersonic region makes the interaction problem complex, and weak waves such as R and T are produced in the strong vortex interaction.

The reflected wave R and the transmitted wave T are too weak to discern clearly in the experiment and the computation, but their contribution is obvious to the quadrupole distribution of density around the circle C ($r = 33$ mm, $r \approx 10r_c$) in Fig. 8d. The T wave cuts the circle at $\theta = 75$ deg, whereas the R wave cuts it at $\theta = 300$ deg, as easily found in Fig. 12. The mean value of density along the circumference is defined as

$$\rho_m = \frac{1}{2\pi} \int_0^{2\pi} \rho \, \mathrm{d}\theta \tag{7}$$

The normalized density $\rho = (\rho - \rho_m)/\rho_m$ instead of the primitive variable is used in Fig. 12. Waves I and T are compression mechanisms [or the density is increased by the wave; denoted (c) in Figs. 12 and 13] and R is the expansion mechanism [or the density is decreased by the wave; denoted (e) in Figs. 12 and 13].

The part of wave A (exactly R, Figs. 7e and 7f) is equivalent to the precursor wave in Ref. 9. For the weak vortex case, the acoustic

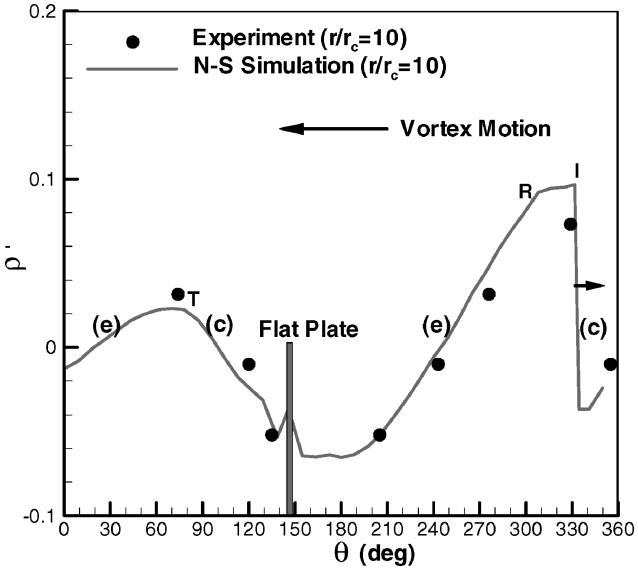

Fig. 12 Density distribution around circle *C* in Fig. 8d: propagating direction of *R* and *T* is left to right.

wave (r_2 in Fig. 4b, for example) is propagated in the radial direction in the cylindrical shape. In Figs. 8c and 8d, the tail of T is extended to C, and T is the acoustic wave in this experimental model (Fig. 8d). In Ref. 9, the precursor and acoustic are attached to the shock front (I and A). In this strong vortex case, however, the tips of R and T are caught in the vortex core for a considerable time due to the strong rotation.

Simplified Model Study

The authors also conducted a simplified model study, the interaction of a planar shock with a modeled vortex, based on Eq. (6), to see the physics clearly because the experiment contains some parasitic waves (A_1 produced by the shock diffraction at the sharp edge of plate, for example). The input parameters are $M_s = 1.22$, $U_{\max} = 420$ m/s ($M_v = 1.22$, the same as $M_{v,\max}$ in the experimental model), and $r_c = 3.3$ mm. The Reynolds number based on $U_{\max}$ and r_c is estimated to be 9.24×10^4.

In Fig. 13a, the incident shock I moving from left to right is distorted by the strong vortex V of clockwise motion. Figure 13b shows tiny R and T. The strong vortex is obviously seen not a as simple circle but as the Arabic numeral eight due to the attachment of weak acoustic waves. The transmitted wave T is the penetration of the impinging shock I through the vortex because they rotate counterclockwise together: Compare Fig. 13c with Fig. 13b. Last, the accelerated wave A and the shock I intersect to form a Mach stem in Fig. 13d. Obviously, the two acoustic waves (one expansion, and the other compression) are emitted from the R (expansion) and T (compression), respectively. After old waves are radiated or split from the original ones, new waves soon grow from the slip layer. Figure 13e is the magnified view of this instant, and it shows the full capacity of the present computational method. The R and T can be discerned in Fig. 13. A schematic diagram for the acoustic emission is given in Fig. 13f.

Overall, this simplified model is a further study of the weak shock and strong vortex case of Ellzey et al.[9] with the addition of new experimental data. However, the strong vortex region should be extended to where the maximum rotational speed is supersonic to understand properly the acoustic emission mechanism such as shown in Fig. 6f. Note that Ellzey et al. called the shock I and A "transmitted shocks" different from transmitted wave T. They also named the branched parts of I and A "reflected shocks." As shown in Fig. 7f, the incident shock I intersects with the accelerated wave A, not the reflected. The present reflected wave (R) indicates the reflection of I in the slip layer of vortex edge.

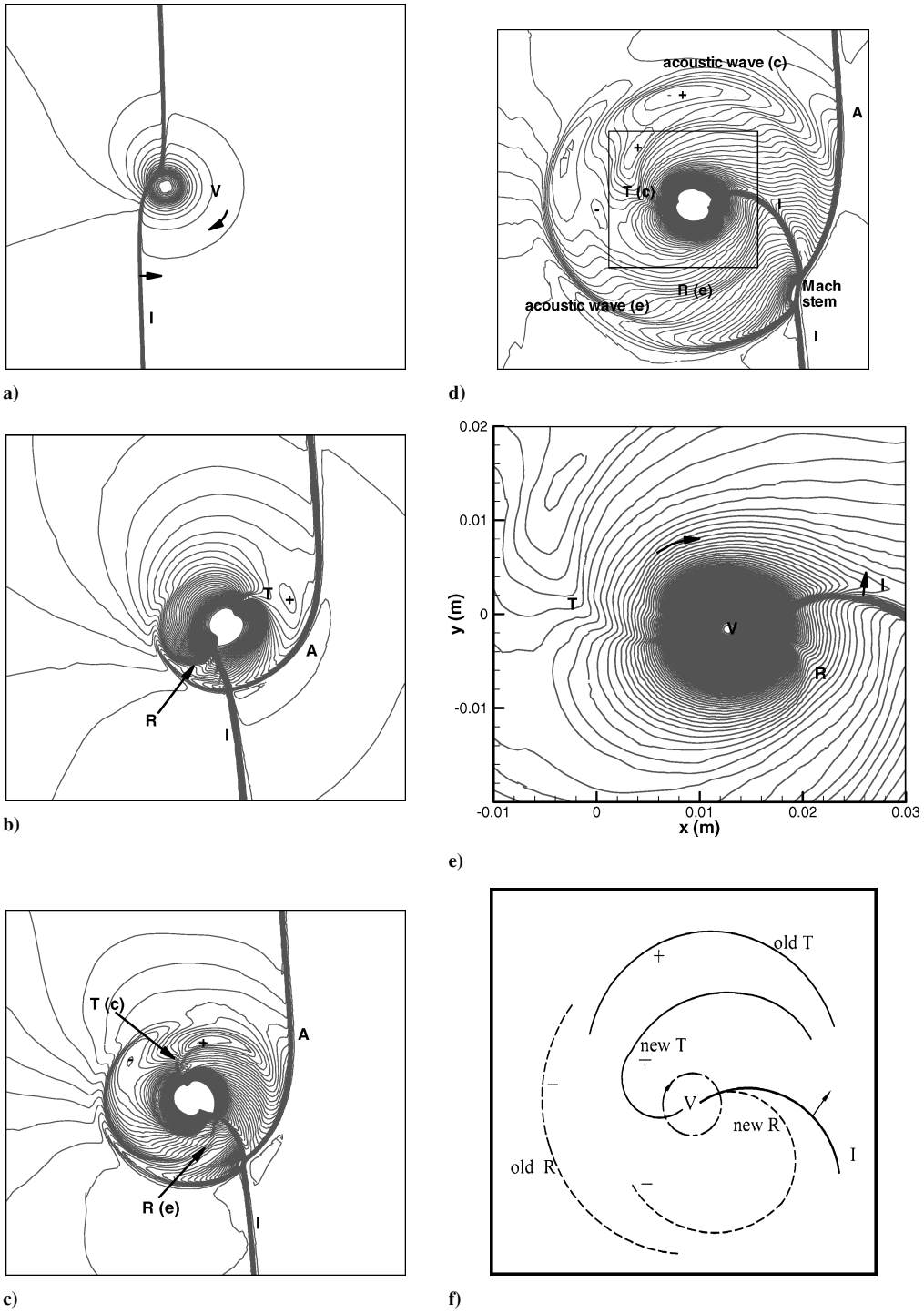

Fig. 13 Simplified model study: a–d) pressure contours along the time sequence, e) magnified view of panel d, and f) schematic diagram for the acoustic wave generation: +, high pressure and −, low pressure.

Summary

The weak acoustic waves, R and T are detected from experimental observation and interpreted with numerical simulation and a simplified model study. They are related to two kinds of physics: shock reflection at the vortex edge and shock penetration through the vortex core. In the present study, it is shown that the two waves play the important role of acoustic wave emission in this weak shock and strong vortex interaction case (Fig. 13f). Using the R and T concept, we can approach on the basic question of what makes acoustic waves in the shock–vortex interaction more feasibly, as well as in a simpler way.

Acknowledgments

This study is financially supported by the Korea Energy Management Corporation (2002-N-WD03-P-01-0-000-2002). The holographic interferogram in Fig. 5c is courtesy of K. Takayama, Tohoku University, Sendai, Japan, http://ceres.ifs.tohoku.ac.jp/∼coe/jachieve2002a.html.

References

[1]Hollingsworth, M. A., and Richards, E. J., "A Schlieren Study of the Interaction Between a Vortex and a Shock Wave in a Shock Tube," Fluid Motion Subcommittee Rept. ARC17985, FM 2323, Aeronautical Research Council, 1955.

[2]Hollingsworth, M. A., and Richards, E. J., "On the Sound Generated by the Interaction of a Vortex and a Shock Wave," Fluid Motion Subcommittee Rept. ARC 18257, FM 2371, Aeronautical Research Council, 1956.
[3]Ribner, H. S., "Convection of a Pattern of Vorticity Through a Shock Wave," NACA Rept. 1164, 1954.
[4]Ribner, H. S., "The Sound Generated by Shock–Vortex Interaction," UTIAS 61, Univ. of Toronto, Toronto, 1959.
[5]Dosanjh, D. S., and Weeks, T. M., "Interaction of a Starting Vortex as Well as a Vortex Street with a Traveling Shock Wave," *AIAA Journal*, Vol. 3, No. 2, 1965, pp. 216–223.
[6]Weeks, T. M., and Dosanjh, D. S., "Sound Generation by Shock–Vortex Interaction," *AIAA Journal*, Vol. 5, No. 4, 1967, pp. 660–669.
[7]Ribner, H. S., "Cylindrical Sound Wave Generated by Shock–Vortex Interaction," *AIAA Journal*, Vol. 23, No. 11, 1985, pp. 1708–1715.
[8]Meadows, K. R., Kumar, A., and Hussaini, M. Y., "Computational Study on the Interaction Between a Vortex and a Shock Wave," *AIAA Journal*, Vol. 29, No. 2, 1991, pp. 174–179.
[9]Ellzey, J. L., Henneke, M. R., Picone, J. M., and Oran, E. S., "The Interaction of a Shock with a Vortex: Shock Distortion and the Production of Acoustic Waves," *Physics of Fluids*, Vol. 7, No. 1, 1995, pp. 172–184.
[10]Chatterjee, A., "Shock Wave Deformation in Shock–Vortex Interactions," *Shock Waves*, Vol. 9, No. 2, 1999, pp. 95–105.
[11]Grasso, F., and Pirozzoli, S., "Shock Wave–Vortex Interaction: Shock and Vortex Deformations, and Sound Production," *Theoretical and Computational Fluid Dynamics*, Vol. 13, 2000, pp. 421–456.
[12]Inoue, O., and Hattori, Y., "Sound Generation by Shock–Vortex Interactions," *Journal of Fluid Mechanics*, Vol. 380, 1999, pp. 81–116.
[13]Chang, S. M., and Chang, K. S., "On the Shock–Vortex Interaction in Schardin's Problem," *Shock Waves*, Vol. 10, No. 5, 2000, pp. 333–343.
[14]Whitham, G. B., *Linear and Nonlinear Waves*, Wiley, New York, 1974, pp. 263–311.
[15]Chang, S. M., "Unsteady Shock–Vortex Interactions in the Compressible Shear Layer," Ph.D. Dissertation, KAIST, DAE965342, Korea Advanced Inst. of Science and Technology, Daejeon, Republic of Korea, 2000.
[16]Ko, S. M., and Chang, K. S., "Resonant Pulsatile Flows of a Hartmann–Sprenger Tube," *CFD Journal,* Vol. 6, No. 4, 1998, pp. 439–452.
[17]de Zeeuw, D., and Powell, K. G., "An Adaptive Refined Cartesian Mesh Solver for the Euler Equations," *Journal of Computational Physics*, Vol. 104, 1993, pp. 56–68.
[18]Quirk, J. J., "An Alternative to Unstructured Grids for Computing Gas Dynamic Flows Around Arbitrary Complex Two-Dimensional Bodies," *Computers and Fluids*, Vol. 23, No. 1, 1994, pp. 125–142.

P. J. Morris
Associate Editor